

SourceREACH (Source REconstruction of Arcs behind Cluster Halos): A New Source Reconstruction Algorithm Optimized for Giant Arcs and Galaxy Cluster Lenses

LANA EID  AND CHARLES R. KEETON 

¹*Rutgers University–New Brunswick,
 Department of Physics and Astronomy,
 136 Frelinghuysen Rd., Piscataway, NJ 08854 USA*

Abstract

We introduce a new algorithm designed for use with extended lensed images, specifically giant arcs lensed by galaxy clusters. These highly magnified images contain important information about both the mass distribution of the cluster and the properties of the background source, but modeling them requires significant computational effort. Our new source reconstruction methodology is designed to be accurate and efficient for high-resolution observations in which point spread function effects are not significant. The overall process deconvolves the observed image by the point spread function, de-lenses the image pixels, and uses interpolation or regression with smoothing to determine the model source. By working with de-lensed points, the method accounts for varying resolution across the source plane. We evaluate the speed and accuracy of different interpolation and regression methods using both mock data and real data for the giant arc in Abell 370. We find that utilizing K Nearest Neighbor Regression results in the best balance of noise smoothing and preservation of compact detail in the source.

Keywords: Strong gravitational lensing (1643) — Gravitational lensing (670) — Abell clusters (9) — Luminous arcs (943)

1. INTRODUCTION

Galaxy cluster lens models inform us about the cluster-scale mass distribution (e.g., Raney et al. 2020a; Diego et al. 2023b; Limousin et al. 2025), possible substructure on a smaller scale (e.g., Diego et al. 2024), and cosmological parameters like the Hubble constant and dark energy from time delays (e.g., Vega-Ferrero et al. 2019; Caminha et al. 2022; Granata et al. 2025; Pierel et al. 2025). Corresponding source reconstruction models facilitate spatially resolved studies of overall source properties, including star formation rate, locations of emission line regions such as Lyman α , and investigations of the smallest scales on which star formation occurs (e.g., Richard et al. 2010; Johnson et al. 2017b; Patrício et al. 2018; Claeysens et al. 2022; Navarre et al. 2024).

Giant, spatially extended arcs crossing critical curves are highly-magnified, multiply lensed extended objects, so they offer us maximum insight into both the source in the early Universe as well as regions producing these images. Studies of both high-redshift source properties (Johnson et al. 2017b; Sharon et al. 2019; Claeysens et al. 2022; Diego et al. 2023a; Fudamoto et al. 2024;

Navarre et al. 2024) and the small-scale lensing dark matter structure effects of milli-lensing (e.g., Niemiec et al. 2023; Diego et al. 2025; Fudamoto et al. 2024; Limousin et al. 2025) rely on the accuracy of multiple-image source reconstructions and the highest magnification regions marked by corresponding critical curves. Microlensing events at critical curves (e.g., Diego et al. 2024, 2025) can contain even higher magnifications than giant arcs overall, and constraining cluster critical curves is crucial for comparing to and interpreting such events.

Recent results, particularly from the Hubble Frontier Fields multi-team modeling efforts (e.g., Raney et al. 2020b; Yang et al. 2020; Eid & Keeton 2025), have demonstrated that these highest magnification regions are still uncertain, with wide variation and systematic uncertainty even among models that generally fit the lensed point-images equally well (Lasko et al. 2023; Galan et al. 2023, 2024b,a; Liesenborgs et al. 2024; Limousin et al. 2025). It is therefore essential to develop a methodology to best constrain these highest magnification regions of cluster models with high-resolution data for giant arcs from the wealth of information we have

now and in upcoming targeted observations and large surveys (Shajib et al. 2025).

Source reconstruction can be done in many forms, including semi-linear inversion, pixel-based, and ray-tracing (e.g., Warren & Dye 2003; Suyu et al. 2006; Veggetti & Koopmans 2009; Tagore & Keeton 2014; Tagore & Jackson 2016; Nightingale & Dye 2015; Diego et al. 2016; Tessore et al. 2016; Karchev et al. 2022; Young et al. 2022; Şengil et al. 2023; Rüstig et al. 2024), forward-modeling with iteratively added complexity (e.g., Yang et al. 2020), and back-projection using a modeled magnification matrix (e.g., Griffiths et al. 2021). Bayesian probabilistic methods are often built into these methods to incorporate uncertainties and regularization; varying source plane resolution can be handled using adaptive gridding techniques, including Delaunay triangulation and Voronoi tessellation.

Techniques for constraining both the lens and background source simultaneously are computationally expensive for cluster-scale models; approaches such as in Birrer et al. (2015); Diego et al. (2016); Birrer & Amara (2018); Yang et al. (2020); Rüstig et al. (2024); Acebron et al. (2024) were tested on separate, multiply lensed, extended images, while the highest magnification regions of interest, which giant arcs cross multiple times, are comprised of merging images that are more computationally expensive to handle as a cluster model constraint.

Recent studies have used lensed arcs to constrain local regions of cluster mass models (e.g., Birrer 2021; Lin et al. 2023; Şengil et al. 2023; Şengil 2025). However, the resulting local mass model may not be valid for the entire cluster due to the focus on more accurately constraining just that region. Lin et al. (2023) show that matching different regions across extended images can adjust local regions of a cluster model without affecting the global properties of the cluster model. We similarly showed this for the case of the giant arc in Abell 370 (Eid & Keeton 2025, hereafter Paper 1), in which we locally optimized a fiducial cluster model from Raney et al. (2020a) using full a pixel-based source reconstruction without significantly affecting the rest of the lensed image position fits or adjusting the cluster-scale matter halos.

Ideally, the entire cluster model would be optimized at once to ensure the best fit for the entire field. We aim to facilitate this with a resource-efficient source reconstruction methodology that we term *SourceREACH* (*Source REconstruction of Arcs behind Cluster Halos*) to work with any set of standard output maps, such as from the Hubble Frontier Fields (Lotz et al. 2017; Yang et al. 2020). We perform a comprehensive study com-

paring different interpolation methods for an updated de-lensing *python* code, prototyped in Paper 1, and we validate our final choice using Hubble Frontier Fields optical data (Lotz et al. 2017).

Section 2 presents the data and mock data used, the code development, and the testing; Section 3 presents our results; Section 4 interprets the results; and Section 5 contextualizes them for future studies.

2. DATA & METHODS:

2.1. The Abell 370 Galaxy Cluster Field

We use data from the Hubble Frontier Fields (HFF) Program (Lotz et al. 2017), which was a 3-year, 840-orbit Hubble Space Telescope (HST) targeting six galaxy cluster fields with the aim of obtaining deep images of the clusters and faint $z \sim 5 - 10$ background galaxies magnified by strong lensing. This survey program is ideal for our study, since it is the base of the various comparison studies that have followed from the lens modeling teams that used the same data to construct their cluster models (e.g., Raney et al. 2020b; Yang et al. 2020).

We focus on the $z = 0.375$ Abell 370 cluster field, which includes the $z = 0.725$ first confirmed strongly lensed galaxy in a giant arc (Soucail 1987; Soucail et al. 1987, 1988). We chose this well-studied system of an extended, giant arc comprised of five merging images of the same background galaxy for our in-depth study of how a high-resolution source reconstruction can be efficiently leveraged as a constraint in order to help address systematic differences between results from diverse cluster modeling methods that persist in the predicted high-magnification regions of interest in these cluster models (Raney et al. 2020b; Galan et al. 2024b).

Paper 1 details the steps we took to isolate the arc and format our inputs for each filter and corresponding data image; we briefly outline them here. The top left panel of Figure 1 shows the data image from the F814W filter, which we used in Paper 1 to optimize the cluster model. In order to isolate the brightness pixels from the giant arc so we can trace them back, we used the *isophote* package from *python photutils* (Bradley et al. 2022) to model and remove the contaminating light from cluster member and other galaxies projected close to the giant arc (upper right panel, Figure 1). Our data mask was created directly in *SAOImageDS9* (Joye & Mandel 2003) using the cleaned, isolated arc image plus a small margin of background, excluding areas with any significant artifacts (lower left panel, Figure 1). For each filter and corresponding data image, we used the *EPSFBuilder* function from the *python photutils* (Bradley et al. 2022) package to create an auto-

normalized “effective PSF” (ePSF) for the filter from an input set of isolated stars in the filter image, which we used to deconvolve the image data from the PSF using Richardson-Lucy deconvolution (lower right panel, Figure 1) (Richardson 1972; Lucy 1974).

2.2. Cluster Lens Model

Multiple lens modeling teams produced publicly-available cluster models for the Hubble Frontier Fields through parametric (Caminha et al. 2017; Jullo et al. 2007; Jauzac et al. 2012, 2014; Richard et al. 2014; Oguri 2010; Ishigaki et al. 2015; Kawamata et al. 2016, 2018; Raney et al. 2020a; Jullo et al. 2007; Johnson et al. 2014), nonparametric (Bradač et al. 2005, 2009; Liesenborgs et al. 2007), and hybrid (Diego et al. 2005a,b, 2007, 2015; Vega-Ferrero et al. 2019) methods with a standard format and calibration.¹

In Paper 1, we began with the 2D fiducial lens model from Raney et al. (2020a,b). That parametric model included 275 mass components: 256 cluster member galaxies, four cluster-scale matter halos representing contributions from both the large dark matter components as well as X-ray gas, and 15 line-of-sight galaxies. It was originally fit to 91 lensed images from 31 image systems in the cluster field. We optimized the model to better fit the giant arc by adjusting the properties of 11 galaxies projected near the arc. That optimization was done using the pixel-based source reconstruction code *pixsrc* (Tagore & Keeton 2014; Tagore & Jackson 2016), which is based on the Suyu et al. (2006) source reconstruction Bayesian formalism.

We only used the F814W filter image for the local optimization, as it had the most structure to fit and the highest signal-to-noise value. Consequently, the fits in the other two filters both improved alongside the red filter, but there is still room for improvement, particularly in the more concentrated, small-scale brightness regions similar to those commonly used as point-image constraints in other source reconstruction (e.g., Johnson et al. 2017a,b).

We note that our cluster lens model remains fixed throughout this paper; no further optimization is done here, as our primary focus is ensuring our source reconstruction code is efficient and accurate as compared to the data and previous source reconstruction methods. As with Paper 1, we focus on the best fit to the F814W data arc. We will next use our source reconstruction code to further optimize the model in a follow-up study.

2.3. Mock Data

¹ <https://archive.stsci.edu/prepds/frontier/lensmodels/>

In addition to using the real data for Abell 370, we also construct a mock arc to serve as a test case for which we know the “truth.” This allows us to determine whether our algorithm provides accurate results and understand how different approaches handle smoothing and noise. This mock arc is created by lensing the best source model from the *pixsrc* analysis. We work with an idealized map with no PSF blurring or noise. We also create a version with Gaussian noise with a standard deviation of 0.0045 (the noise level used in the previous *pixsrc* analysis). This corresponds to a peak signal-to-noise ratio of approximately 18.

2.4. Source Reconstruction Algorithm

Our source reconstruction algorithm, which we construct in *python* for testing, is a straightforward de-lensing code for high-resolution data sets in which atmospheric and optical blurring can be removed through PSF deconvolution. The general workflow of the code is as follows:

1. Deconvolve the image from the point spread function (PSF) using Richardson-Lucy deconvolution.
2. De-lens the image by mapping all of the image plane pixels back to the source plane using the input deflection maps. The resulting set of brightness points will have irregular spacing. In order to preserve the varying resolution of the source from different parts of the giant arc and not introduce any extra systematics, we work with solely this set of points.
3. Perform the desired smoothing routine, either 1) an interpolation with smoothing or 2) a function trained on the data values that then predicts values at those same positions.
4. Re-lens the new brightness values in the source plane to their deflected image plane positions, and convolve with the PSF to obtain the model image. A single χ^2 value from these image plane residuals can then be used as a constraint for optimizing a cluster model.

A critical part of source reconstruction is handling noise; this often involves some form of smoothing or regularization to avoid overfitting. Vernardos & Koopmans (2022) examine different approaches to regularization, including physically-motivated priors, in order to break degeneracies in under-constrained lens modeling and source reconstruction. This works to avoid overfitting and ensure that differential magnifications in different regions of the source are handled properly (Tagore

Abell 370 Giant Arc
F814W Data Image Preparation for Source Reconstruction

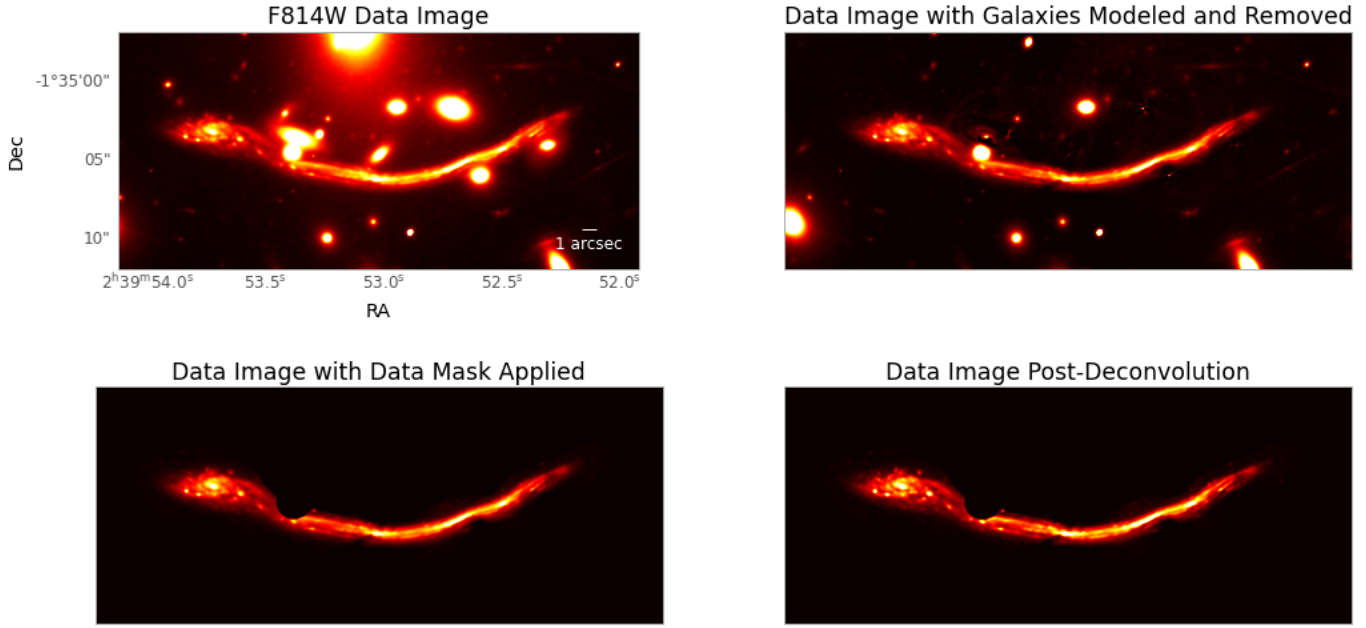


Figure 1. **Top left:** Data image created from the HST F814W filter from the Hubble Frontier Fields program. **Top right:** Data arc with light from galaxies near the arc modeled and subtracted (except for two along the left portion of the arc, which were masked instead; see Paper 1 for more discussion). **Bottom left:** Masked and cleaned data arc, which was the input to *pixsrc* for our previous optimization runs. **Bottom right:** Cleaned and masked data arc after deconvolution with the Richardson-Lucy algorithm.

& Keeton 2014; Tagore & Jackson 2016; Vernardos & Koopmans 2022; Young et al. 2022). Regularization may overly smooth these features if not done carefully because it avoids large changes when aiming for a smooth source. Compact regions, such as star forming knots, are sometimes explicitly used in lens modeling, such as in the previous analysis of Abell 370 by Richard et al. (2010); Patrício et al. (2018), though their source reconstruction only utilized the least magnified, least warped, leftmost arc image.

Our approach uses interpolation or regression functions in the source plane to provide adaptive smoothing. We examine the following methods:

- **Radial Basis Function Interpolation:**² This interpolation algorithm constructs functions defined as the distance between inputs and fixed centers and interpolates using their weighted sum. The radial basis function can be chosen as a polynomial of desired degree for different levels of detail.

² Implemented as *scipy.interpolate.RBFIInterpolat*or (Virtanen et al. 2020).

- **K Nearest Neighbor Regression:**³ This supervised machine learning algorithm predicts the value at a given point by averaging the values of the K nearest neighbors.

- **Decision Tree Regression:**⁴ This supervised machine learning algorithm recursively partitions the input data to fit smaller sections. It minimizes the error by identifying a branching threshold at which to form leaves that it averages to fit each value.

- **Random Forest Regression:**⁵ This ensemble machine learning algorithm averages conclusions from multiple decision trees to avoid overfitting. Each tree is trained on a randomly selected and bootstrapped section of the data, and it recursively splits the inputs at a given threshold to minimize error and predict values.

³ Implemented as *sklearn.neighbors.KNeighborsRegressor* (Pedregosa et al. 2011).

⁴ Implemented as *sklearn.tree.DecisionTreeRegressor* (Pedregosa et al. 2011).

⁵ Implemented as *sklearn.ensemble.RandomForestRegressor* (Pedregosa et al. 2011).

For each method we test different inputs and options, including parameters such as the number of nearest neighbors, number of estimators, and minimum leaf size in order to best balance smoothing noise in the source with ensuring that the source is complete.

In order to evaluate the accuracy and efficiency of each smoothing and prediction method, we utilize the root-mean-squared (RMS) value of the residuals between the data and model, computed in both the image plane and source plane. For the image plane, we only compute the RMS within the data mask.⁶

3. RESULTS

3.1. Initial Results: Mock Data

We first use our mock arc to test source reconstruction with reasonable inputs for each of the four smoothing methods. Figure 2 shows results for the idealized mock arc with no noise, while Figure 3 shows the corresponding results for the noisy mock arc.

We can see in the idealized mock arc that each of the smoothing functions performs slightly differently for the more compact regions, though the most smoothing occurs within the caustic region. This is because the inner caustic region is what ends up being lensed into the more points, so when the de-lensing occurs, more points and more noise naturally end up in that now higher resolution region of our source.

The noisy mock arc differs more for how each of the smoothing functions handles the noise in the galaxy versus the background regions, as the more visible source residuals show where more smoothing occurred. It is important to balance not overfitting noise with not adding extra predicted noise in the model arc.

3.2. Real Data: Smoothing Methods

We now compare these four interpolation routines with various inputs relating to smoothing for the real data in the HFF F814W filter. We select options for each smoothing method that avoid overfitting the de-lensed noise and that run on the order of a few seconds.

3.2.1. Radial Basis Function Interpolation

Radial Basis Function Interpolation uses the input data as control points to form a set of curved spline functions that provide a smoothed fit to the overall structure.

⁶ In Paper 1, in order to accommodate the different model arc extents, we constructed from the HFF deflection maps from each team, we previously calculated the RMS within a slightly larger rectangular region with extra zero values. Here, we work strictly within the data mask valid for the arcs produced by our models with no extra values. The residual RMS for the F814W filter source reconstruction was 3.53×10^{-4} in Paper 1; strictly within the data mask, we now calculate it as 2.19×10^{-3} .

We test the default Thin Plate Spline mode as well as Linear and Cubic modes to test how different levels of complexity and smoothing fit the compact versus global regions without over-smoothing them, as is often the issue in noise handling.

Our results are shown in Figure 4. We use an input neighbors number of 6, and we choose a smoothing parameter of 0.25, which we found to have the best balance of not overfitting noise but still providing smoothing. We find that the Linear option performs best for the more compact regions, corresponding to star forming clumps, to give us smaller residuals there; this is possibly because of how the noise ends up being handled better globally with the lower degree radial basis function. Each option has similar residuals in the inner caustic regions as seen before in the first test of the other methods. We choose this Linear option as the best version of this function, especially since the RMS in the image plane residuals are lower for this setup.

3.2.2. K Nearest Neighbors Regressor

The K Nearest Neighbors method looks at a chosen number of input pixels around each data point and uses the average of those surrounding pixels to predict the value of the desired point. By design of explicitly utilizing the surrounding region of a given number of points in our scattered, de-lensed data, this works to prevent excessively large gradients or breaks in the data along that varying resolution.

The K Nearest Neighbor Regression method performs the fastest in our tests. As before, we choose the input number of nearest neighbors as 6 for consistency and not overfitting noise; we additionally test 18 nearest neighbors to check how including more points affects the results for varying resolution regions. For all these tests, in order to ensure smoothing not overfitting noise, we use the uniform-weighted option, as opposed to the distance-weighted.

Our results comparing data organization options are shown in Figure 5. This method has two main options to organize the data: 1) Ball Tree, which recursively partitions data regions into hyperspheres centered around pivotal or important points in the data, and 2) KD Tree, which recursively partitions data regions into k-dimensional space while doing the parameter search. The Ball Tree method is slightly faster and better suited for organizing large datasets than the KD Tree method, which is evident in the smaller RMS in the image plane residuals for the former method. Besides speed, the Ball Tree is also better suited for fitting the smaller-scale data while ensuring smoothness. Considering this as well as its lower RMS in the image plane residuals, we

Interpolation and Regularization Type Comparison

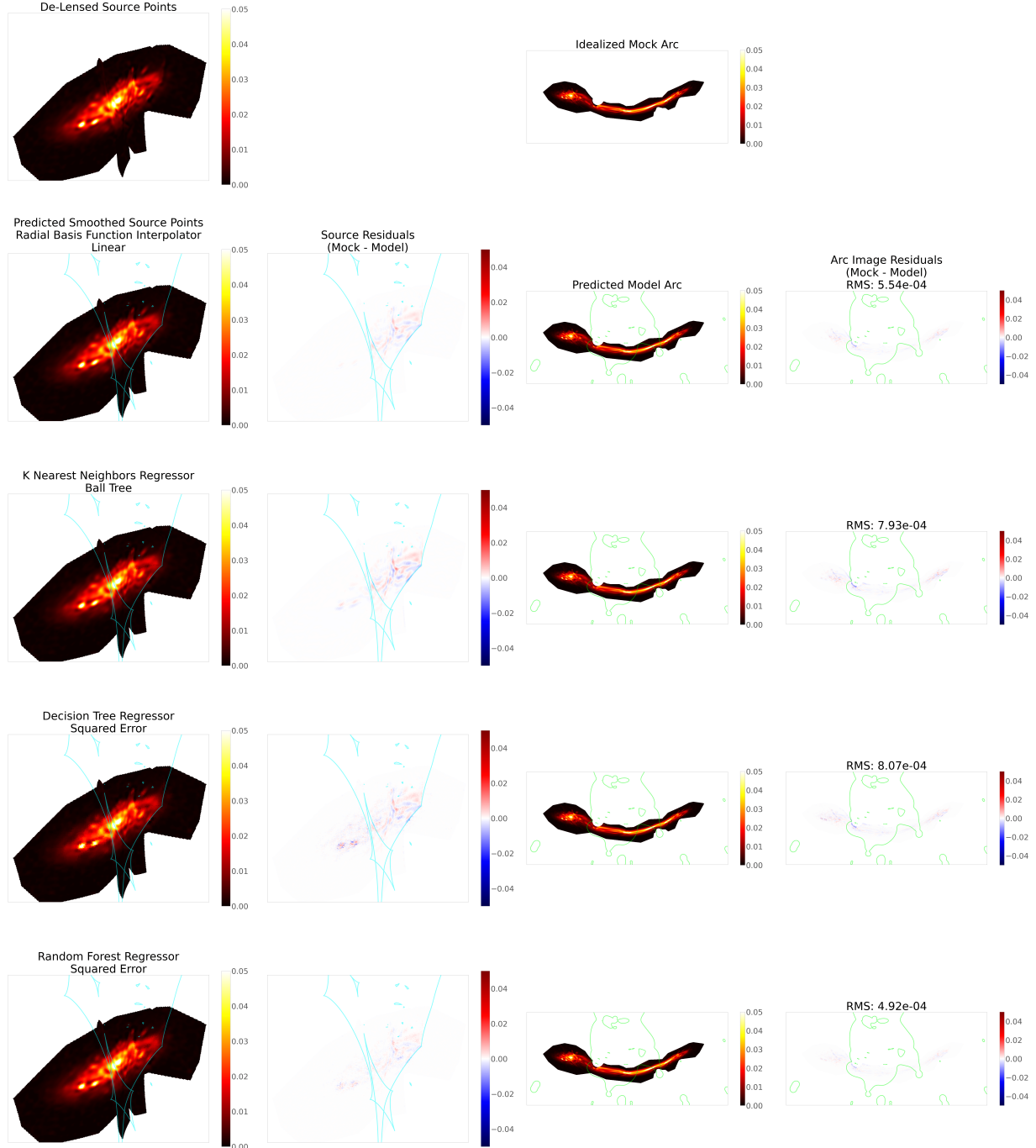


Figure 2. Results from our de-lensing source reconstruction applied to the idealized mock arc with no noise and no PSF. **Top Row:** De-lensed source prior to smoothing and isolated mock arc. **Remaining Rows:** Smoothing method tests on the same set of pixels as above: Radial Basis Function Interpolation, K Nearest Neighbors Regression, Decision Tree Regression, and Random Forest Regression. **First Column:** Model source, with lensing caustics overlaid for reference. **Second Column:** Residuals between the model source and the de-lensed input points. Caustics overlaid for reference. **Third Column:** Model arc created from the smoothed source. Critical curves overlaid for reference. **Fourth Column:** Residuals between the model arc and the mock data; RMS is calculated within the data mask region. Critical curves overlaid for reference.

Interpolation and Regularization Type Comparison

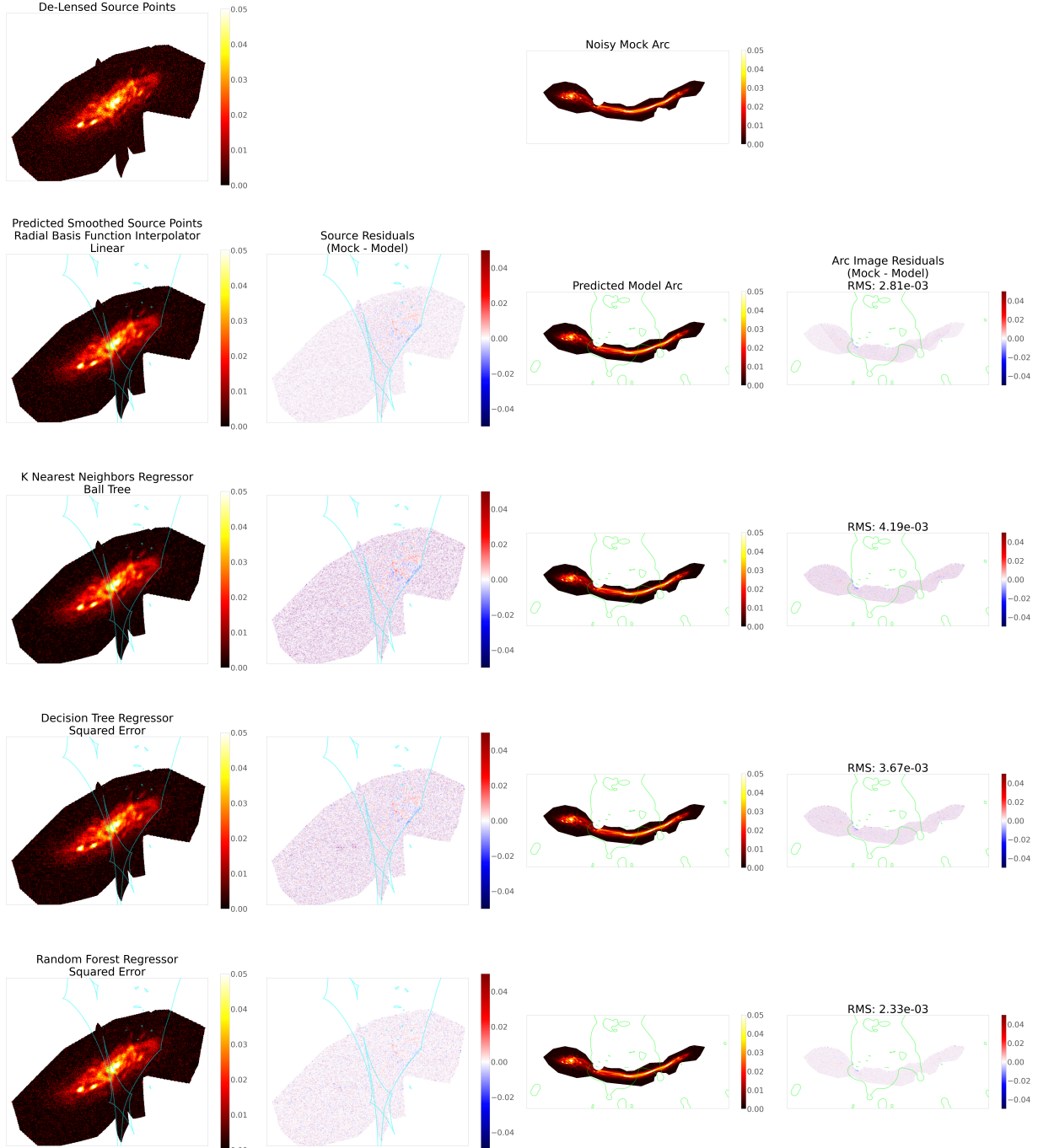


Figure 3. Similar to Fig. 2 but for the noisy mock arc with no PSF.

Radial Basis Function Interpolator

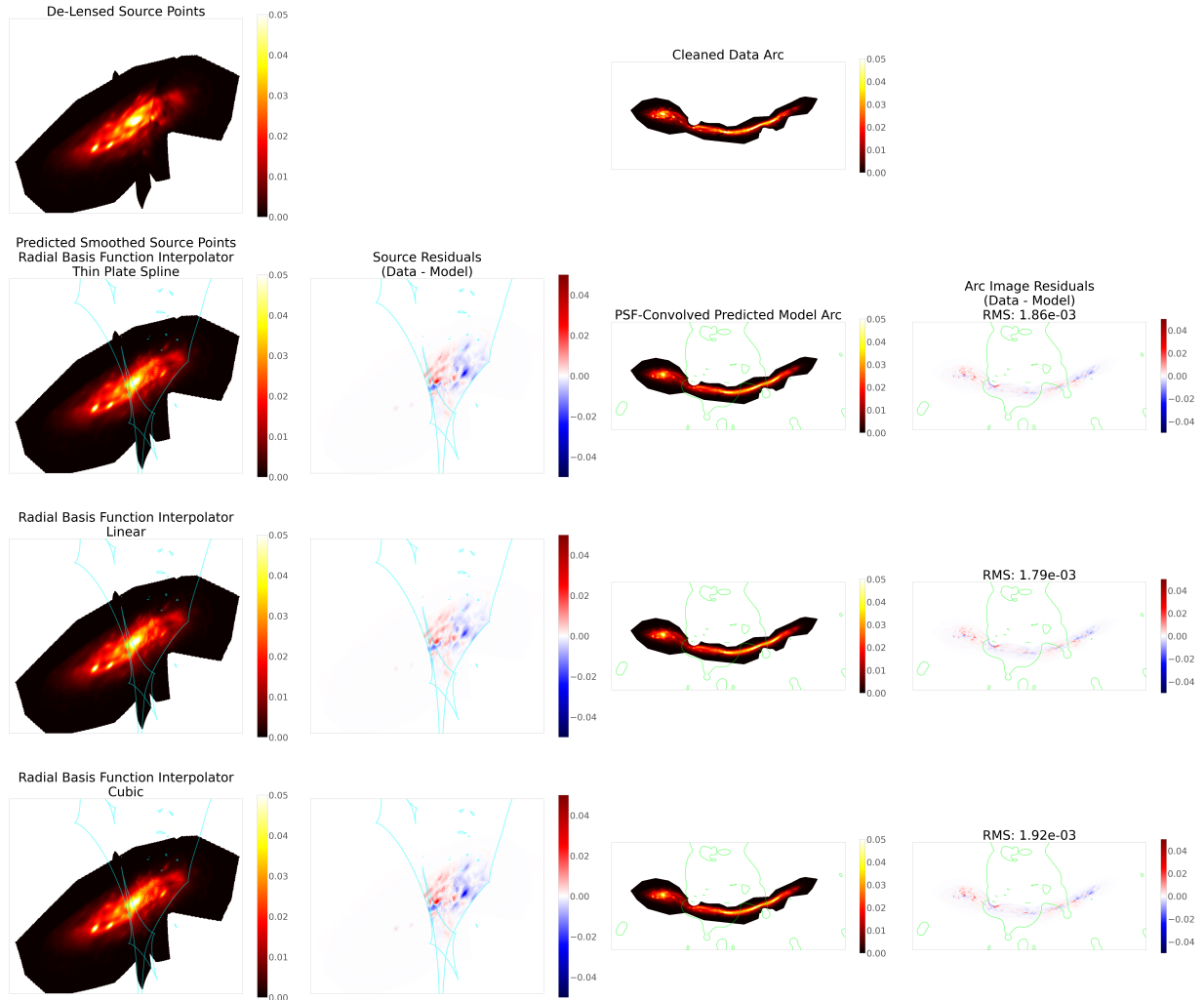


Figure 4. Results from our de-lensing source reconstruction applied to the cleaned data in the F814W filter for the observed arc in Abell 370. The structure of the figure is the same as in Fig. 2; note that here we compare the PSF-convolved model arc to the cleaned data arc. Here we focus on Radial Basis Function Interpolation with different options.

therefore choose the KNN Ball Tree method as the best input option for this function.

We next test this option for different numbers of neighbors. We show this result in Figure 6. Lower numbers of neighbors would fit smaller features well, but setting them too low runs the risk of overfitting noise. Higher numbers of neighbors, by contrast, may smooth out the smaller-scale features in the spiral arms of the source galaxy.

Our previously used value of 6 for the number of neighbors is the best suited for ensuring we do not over-smooth the compact features but that we do still perform reasonable noise smoothing.

3.2.3. Decision Tree Regressor

Decision Tree Regression is a form of organizing the data by splitting it into branches that each have leaf

nodes, which each represent a prediction formed from the mean of those values within the leaf. It begins with higher-level structure and moves down to smaller structures to define. One of the defining options we can adjust and test is the minimum samples to form a leaf node, which sets the level of finer detail to include in each prediction; increasing it will consequently smooth out noise.

Our results are shown in Figure 7. As with the previous function, we choose a single value for the minimum samples to form a leaf as 6, and we test two different criterion options, Squared Error and Friedman Mean Squared Error, that determine when the function splits the data into branches; the other options did not perform well for our data. We can see that there is more smoothing done in regions outside of where the other

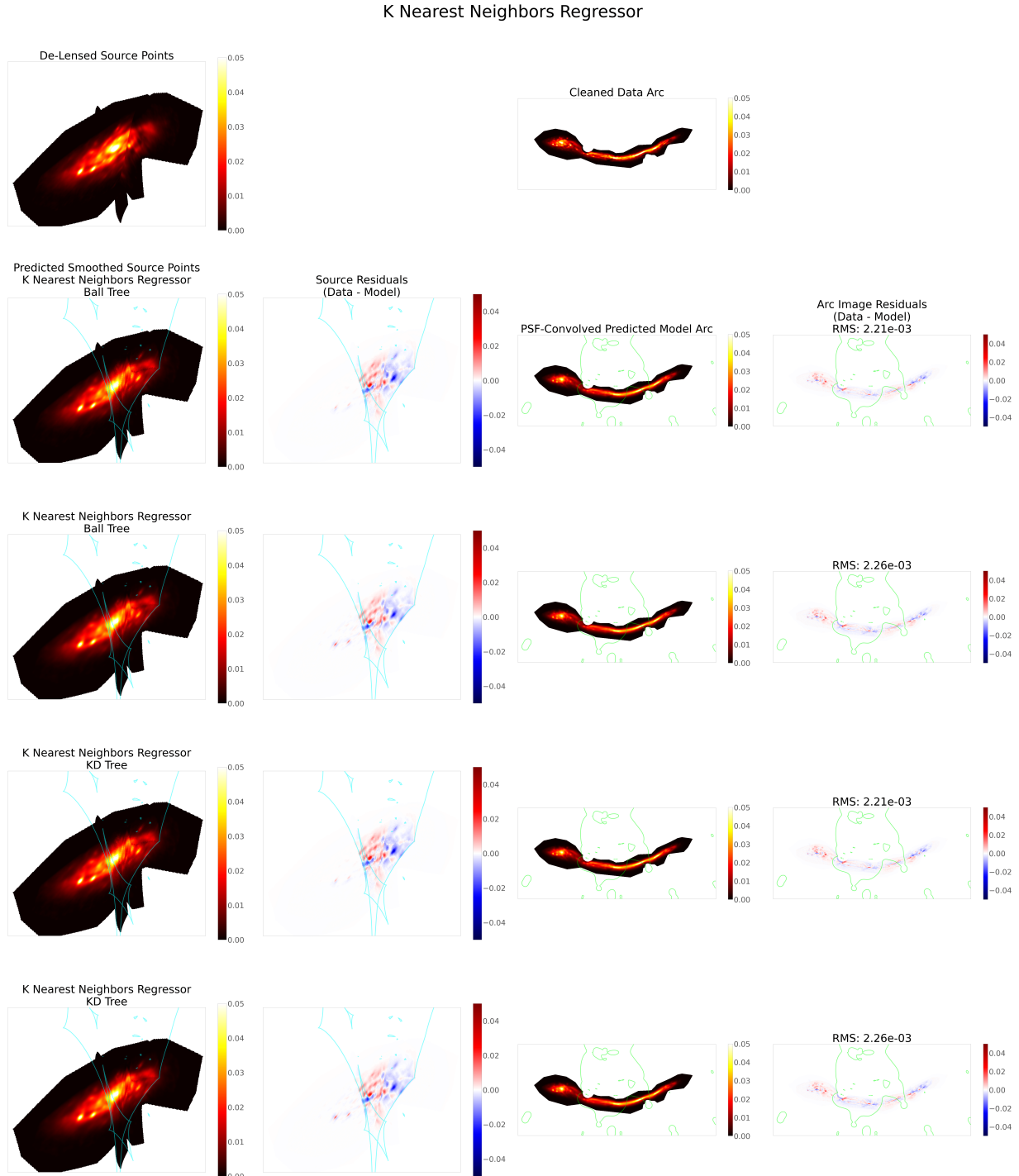


Figure 5. Similar to Fig. 4 but for different organization routine options for K Nearest Neighbors Regression.

KNeighborsRegressor Number of Neighbors Value Comparison

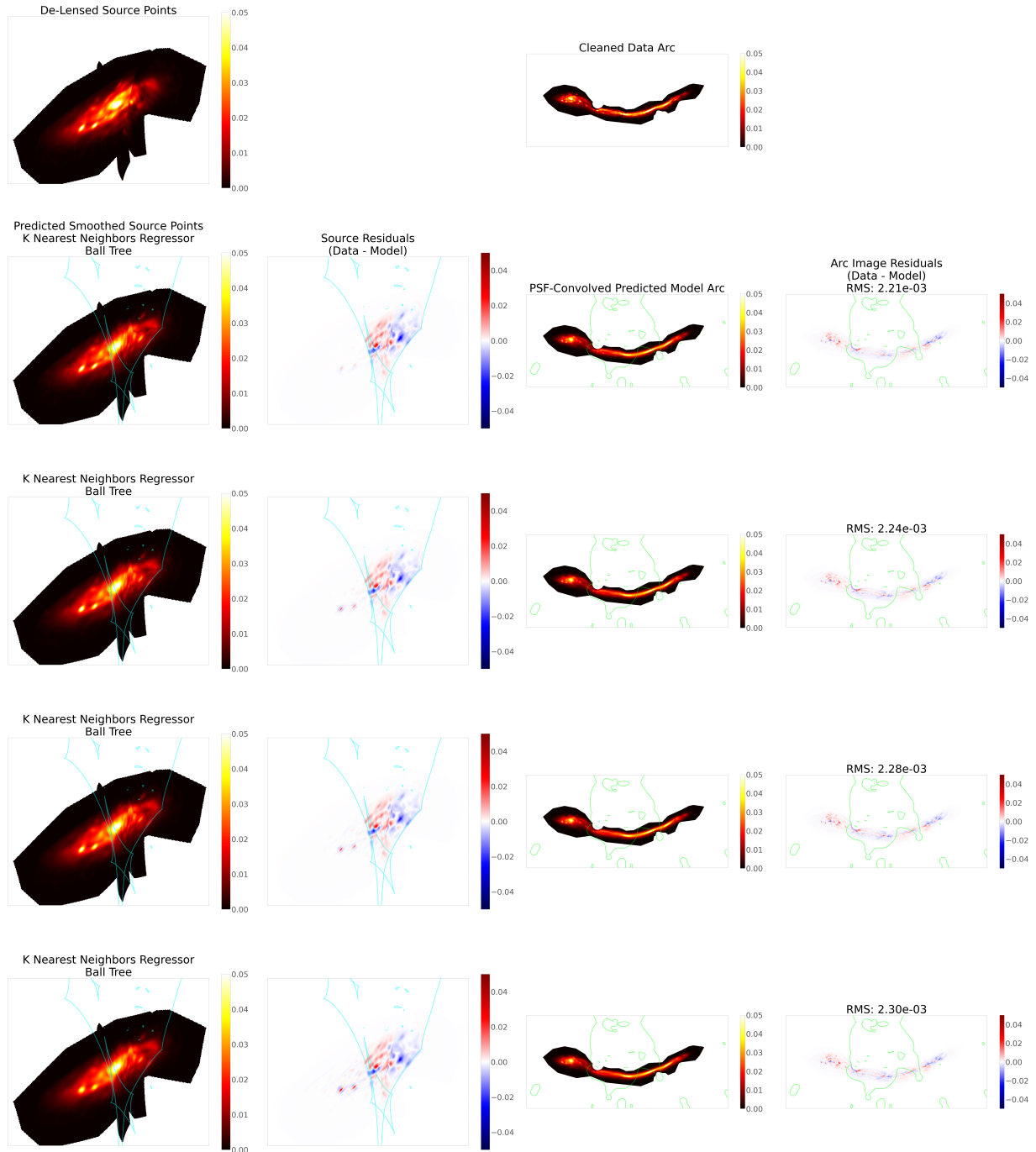


Figure 6. Similar to Fig. 5 but for the K Nearest Neighbors Ball Tree smoothing option with a varying number of neighbors. The best option for dealing with the scattered de-lensed noise was 6 nearest neighbors.

functions we tested had smoothing, and this shows up in the overall slightly higher RMS in the image plane residuals. These options both perform similarly, so we choose the Squared Error version for comparison with the other methods.

3.2.4. Random Forest Regressor

Random Forest Regression builds on the Decision Tree Regression method by averaging the predictions of an assembled forest of decision trees, each structured as above and with its own full set of predictions. It also uses bootstrapping, which resamples different versions of the data to work against overfitting the statistical noise. The two quantities that we choose to vary are the minimum leaf size, defined above, and the number of estimators, which represents the number of decision trees in the random forest.

The benefit of utilizing multiple decision trees is a lower chance of overfitting noise while still maintaining overall structure of the data. We do indeed see more smoothing, less overfitting of noise, and a more reasonable resolution with the Random Forest Regression method as compared to the Decision Tree Regression method.

Our results are shown in Figure 8. Similar to before, we test two criteria for the function to split the data into branches, Squared Error and Friedman Mean Squared Error, with both 6 as the minimum leaf size as well as 6 for the the number of estimators to understand their effects on the fit. We see that the panels with the smaller input number of estimators perform better than the smaller minimum leaf size if we compare RMS residuals in the image plane. We therefore choose the Mean Squared Error criterion with the 6 number of estimators as our best version of this function, since that is where it does less smoothing in the regions where we expect the source to not need much smoothing.

3.3. Final Choice of Method

We choose the inputs from each category with the best balance of source smoothness and image plane residual RMS to test on the data arc again in our comparison Figure 9. All of the methods and options we chose in the aforementioned *python* functions were chosen to have interpolation times on the order of a few seconds for our $\sim 104,000$ pixel, data masked input arc.

Based on visual inspection, low RMS residuals, smoothness, and reasonably short run time, the K Nearest Neighbors routine with the Ball Tree option and a reasonable number of nearest neighbors for this data offers the most reasonably smoothed and reconstructed source. We note that the ideal number of neighbors

value will be different for each data set based on resolution and amount of noise; we will further investigate how to best determine this based on resolution in our follow-up study when we constrain our cluster model with this source reconstruction code. Ensuring the smoothing method takes a short amount of time is critical in order to use the de-lensing code as a constraint in a parameter optimization search for cluster modeling.

4. DISCUSSION

In order to produce a comparison to our RGB image in Paper 1, we perform the de-lensing source reconstruction with the F814W, F606W, and F435W filters from the HFF. The red filter has the least noise to handle, but the green and blue filters have more significant structure in their noise that was more difficult to smooth out. The blue filter especially had noise levels comparable to the signal.

The distribution of the brightness peaks and extended structure in each filter varies, as each originates from a different region, such as the center of the spiral galaxy being redder and more extended, the star forming clumps being bluer and more concentrated, and the green filter being an intermediate example between the two.

We use the same input settings of 6 nearest neighbors for the KNN Ball Tree option to obtain the source reconstructions, shown in Figure 10.

This comparison figure to the results from Paper 1 shows that the source reconstruction performs similarly well and has similar structure in the regions that can still be optimized further in the cluster model, such as the caustic boundaries and the smaller-scale structure. We compare the RMS in the residuals in Table 1. We recomputed the RMS values strictly within the displayed data mask for side-by-side comparison.

HST Filter from HFF	RMS <i>PixSrc</i>	RMS <i>SourceREACH</i>
F814W	2.189×10^{-3}	2.186×10^{-3}
F606W	2.073×10^{-3}	2.691×10^{-3}
F435W	8.436×10^{-4}	7.563×10^{-4}

Table 1. Comparison of RMS values for F814W, F606W, and F435W filters between the previous *pixsrc* analysis and the new *SourceREACH* analysis.

Looking at the source residuals columns in the simplified models in Figure 2 and Figure 3, we can see that the source smoothing happens in regions with compact brightness sources, such as star forming clumps, and especially within the caustic region. This is even more apparent in the source residuals columns in the full data

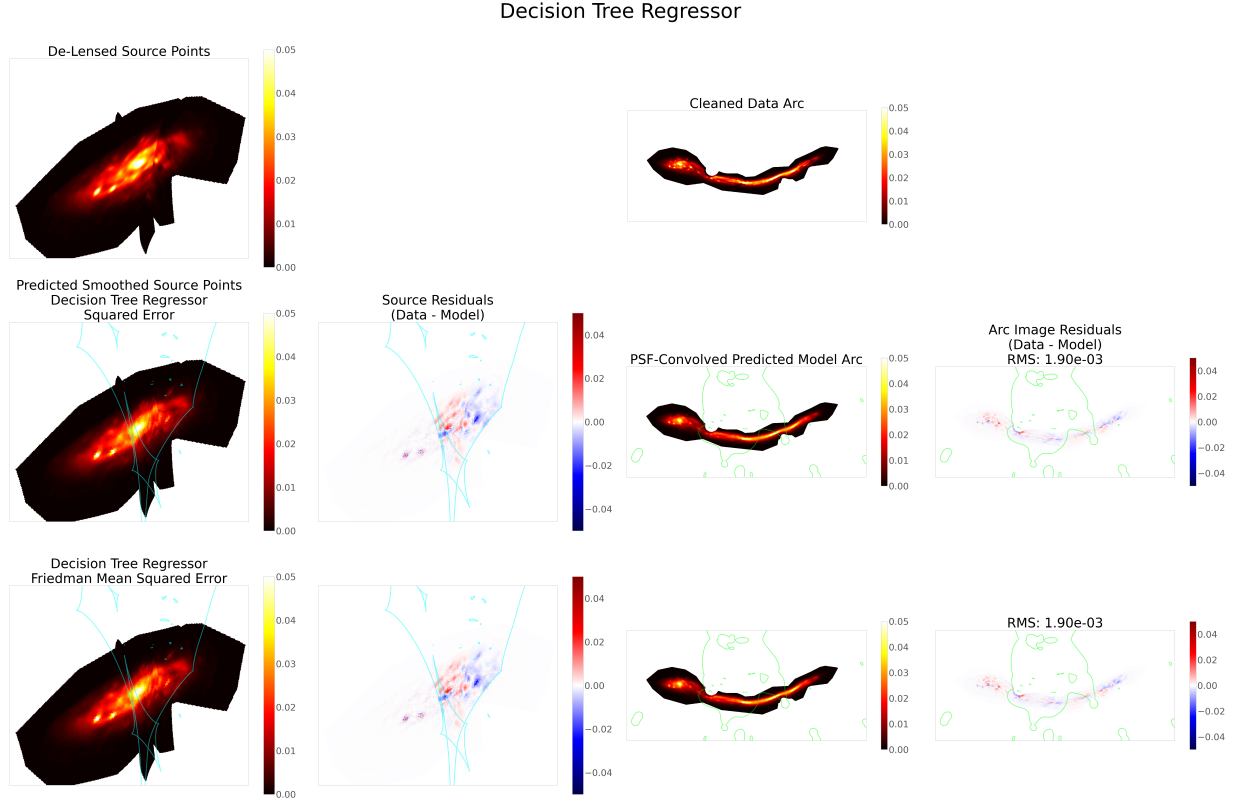


Figure 7. Similar to Fig. 4 but for different interpolation routine options for the Decision Tree Regression method.

from Figure 9. The model arc with added Gaussian noise showed more differences between how each function smoothed the noise in the background areas and showed a similar structure in the residuals.

Considering the arc residuals in corresponding figures, we see that there is some structure in the residuals near the galaxies that we were previously (Paper 1) unable to remove and simply masked for our source reconstructions. This can further be improved in the future by more accurately modeling and masking the galaxies, perhaps with higher resolution data as well. The residuals show a similar pattern to what we saw in Paper 1, where the F814W source reconstruction fits the larger-scale brightness regions better, and the F814W and, more so, the F435W filter source reconstructions have structure in the residuals near the star forming clumps represented by more compact brightness regions. Since this is all done using our locally optimized model from Paper 1, we anticipate that once we include the source reconstruction in one or all filters as a constraint in the cluster model from the start, we may be able to improve these residuals and gain an even more accurate source reconstruction and cluster model, especially for this region, while affecting the fit of the global point images even less than we previously did with our optimization.

5. CONCLUSIONS & FUTURE WORK

We have introduced a new source reconstruction methodology called *SourceREACH* that can efficiently de-lens and interpolate giant arcs lensed by galaxy clusters. This method uses the full, pixelized giant arc information in a short interval of time, which is crucial for folding in the extended image fit as a constraint in cluster modeling.

The smoothing method, whether interpolation or regression, must be chosen carefully, as something that has too-small of a residual RMS will actually overfit the de-lensed noise, and some options may end up smoothing out features of interest such as star forming clumps or transient events. Our choice ended up being a close decision between several functions that performed very similarly, but the identification of the K Nearest Neighbors Ball Tree technique as the ideal method was informed by testing each on multiple filters and quantifying where and why certain issues occurred in each fit.

We will next use *SourceREACH* to update lens models for Abell 370 that simultaneously incorporate constraints from the giant arc and the abundance of compact lensed images. Our methodology could also be valuable for upcoming large surveys that include cluster lenses, such as Euclid (Euclid Collaboration et al. 2025) and LSST (LSST Science Collaboration et al. 2009; Sha-

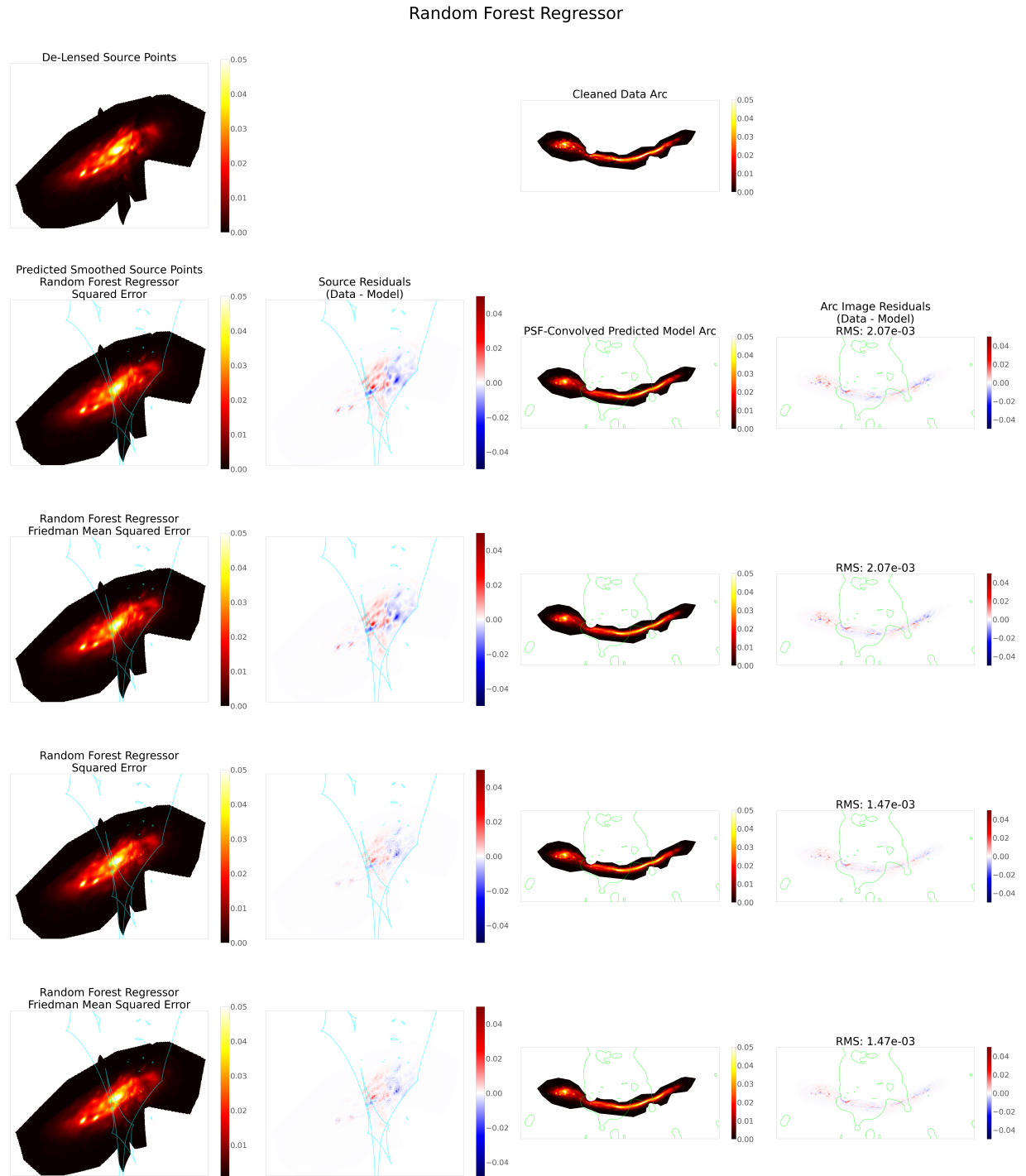


Figure 8. Similar to Fig. 4 but for different interpolation routine options for the Random Forest Regression method.

Interpolation and Regularization Type Comparison

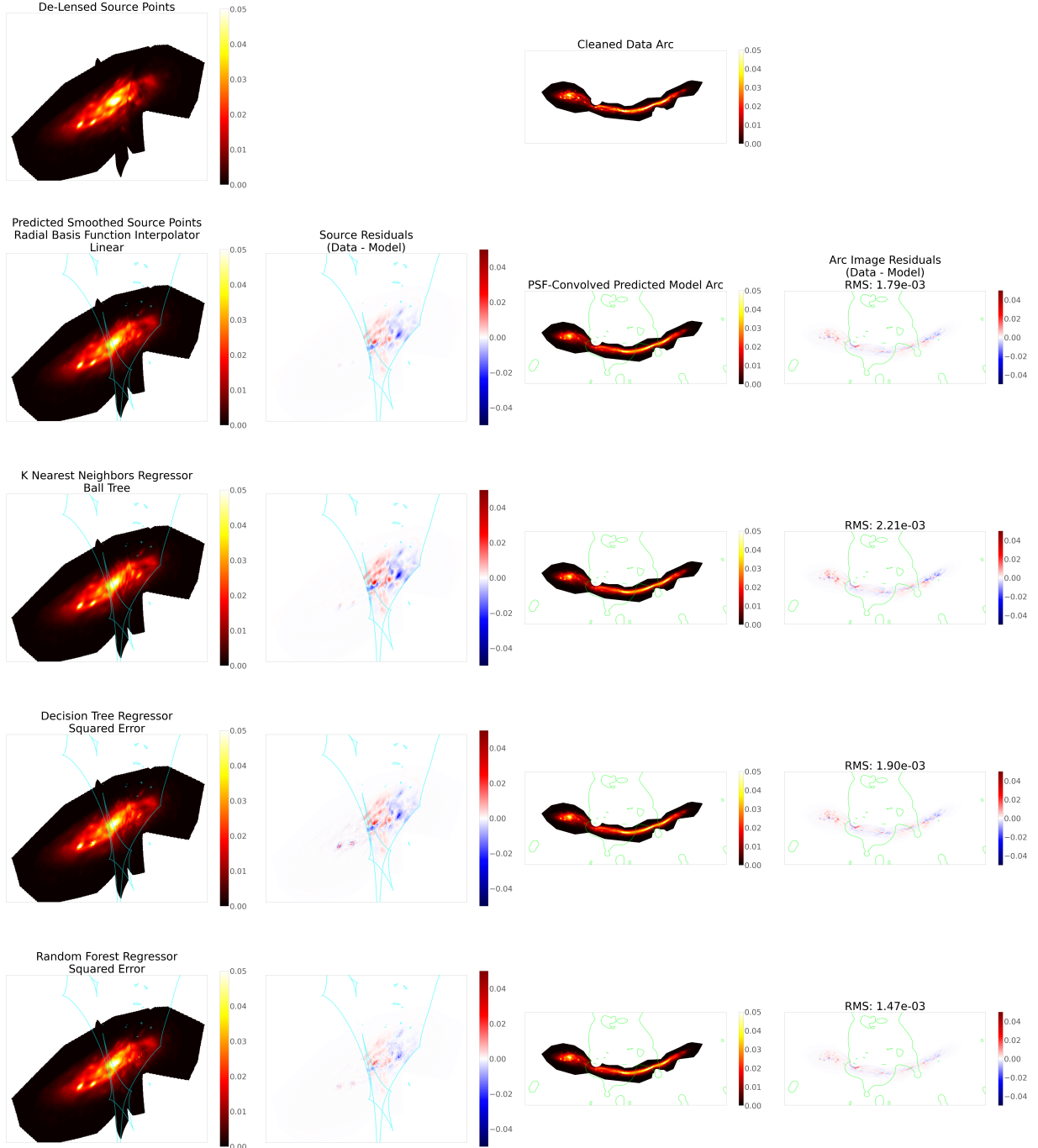


Figure 9. Similar structure as Fig. 4. Shown here is a set of the best input options from each of the interpolation tests for our source reconstruction code. This is done using the the data arc and previously optimized model after deconvolving the HFF F814W filter data from the corresponding PSF.

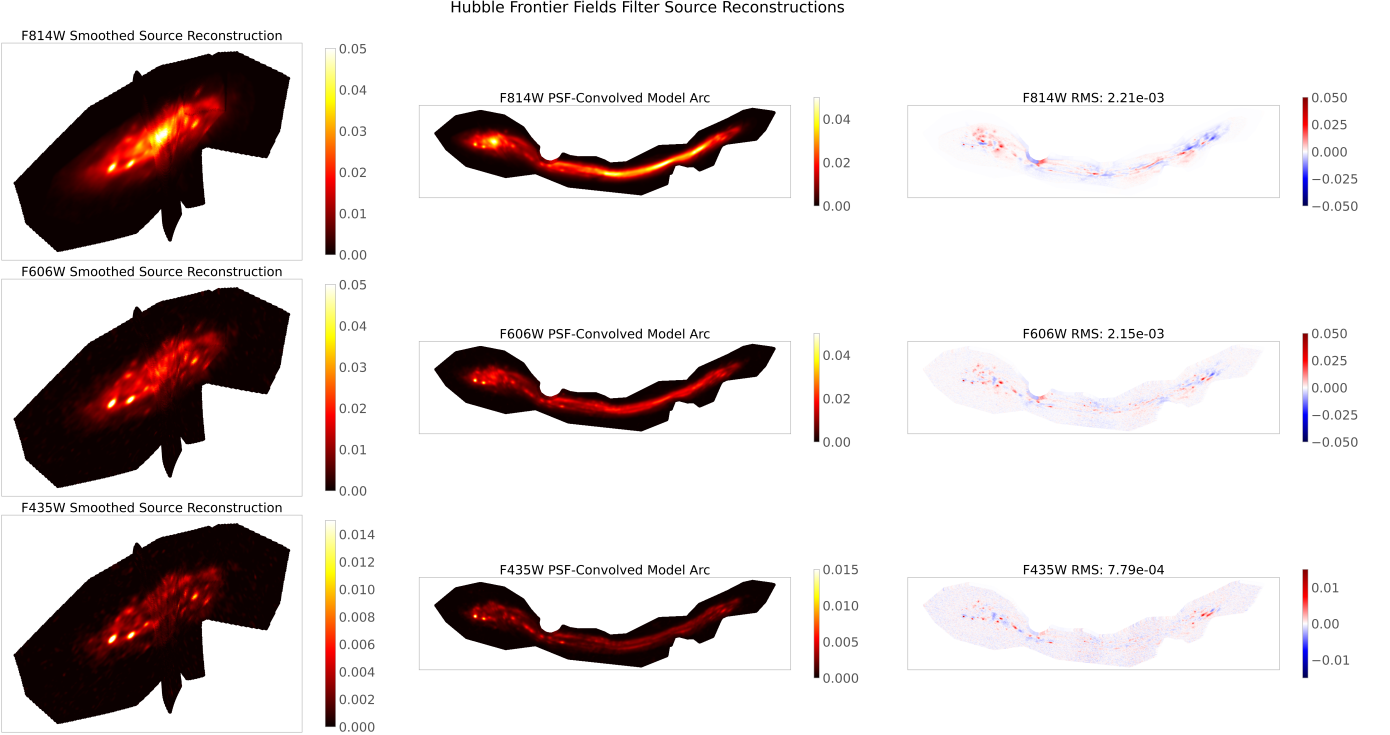


Figure 10. Abell 370 data arc source reconstruction for the HFF F814W, F606W, and F435W filters, predicted and smoothed with the KNN Ball Tree option with 6 nearest neighbors. We display here the source reconstruction in the left column, the reconvolved model arc in the middle column, and the residuals showing deconvolved data minus model arc with no PSF reconvolution in the right column.

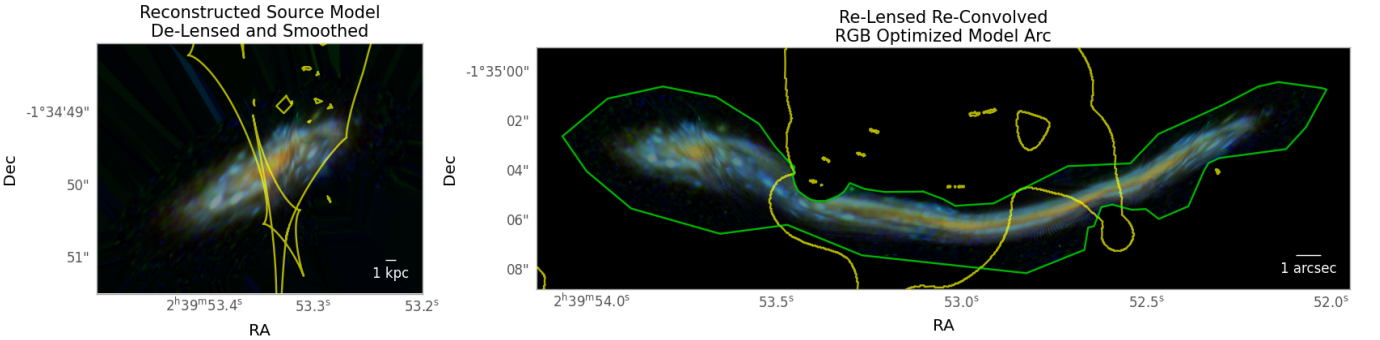


Figure 11. **Left:** RGB source reconstruction using the F814W, F606W, and F435W HFF filters. Corresponding caustics are overlaid in yellow; a 1 kpc scale bar is shown for reference. **Right:** Model arc created using source reconstruction and reconvolved with PSF in each filter. Corresponding critical curves and data mask are overlaid in yellow and green, respectively; a 1 arcsecond scale bar is shown for reference.

jib et al. 2025), where the data may not be as focused as for the Hubble Frontier Fields (Lotz et al. 2017) or CANUCS and other surveys with JWST (Diego et al. 2024, 2025; Sarrouh et al. 2025) but may contain interesting systems that would need in-depth, efficient analysis to determine when transient events (e.g., Diego et al. 2024; Frye et al. 2024) may be observed in follow-up studies without needing separate, higher-resolution observations first. We will investigate this in our future work.

Overall, it is important not to ignore the full information present in high-resolution, extended giant arcs lensed by galaxy clusters, as they provide information that cannot be assumed from point-image fitting in a straightforward manner. The de-lensing methodology presented here is a step forward in ensuring we can easily utilize the source reconstruction of these critical curve-crossing lensed images and fully describe the cluster region causing these maximally magnified images as well as the source itself in accurate detail.

ACKNOWLEDGMENTS

We acknowledge financial support from the Rutgers - New Brunswick Department of Physics & Astronomy. We also thank José María Diego, James Nightingale, Giovanni Granata, and Huimin Qu for helpful discussions.

DATA AVAILABILITY

REFERENCES

- Acebron A., et al., 2024, *ApJ*, 976, 110
- Birrer S., 2021, *ApJ*, 919, 38
- Birrer S., Amara A., 2018, *Physics of the Dark Universe*, 22, 189
- Birrer S., Amara A., Refregier A., 2015, *ApJ*, 813, 102
- Bradač M., Schneider P., Lombardi M., Erben T., 2005, *A&A*, 437, 39
- Bradač M., et al., 2009, *ApJ*, 706, 1201
- Bradley L., et al., 2022, astropy/photutils: 1.5.0, doi:10.5281/zenodo.6825092, <https://doi.org/10.5281/zenodo.6825092>
- Caminha G. B., et al., 2017, *A&A*, 600, A90
- Caminha G. B., Suyu S. H., Mercurio A., Brammer G., Bergamini P., Acebron A., Vanzella E., 2022, *A&A*, 666, L9
- Claeyssens A., et al., 2022, *A&A*, 666, A78
- Diego J. M., Protopapas P., Sandvik H. B., Tegmark M., 2005a, *MNRAS*, 360, 477
- Diego J. M., Sandvik H. B., Protopapas P., Tegmark M., Benítez N., Broadhurst T., 2005b, *MNRAS*, 362, 1247
- Diego J. M., Tegmark M., Protopapas P., Sandvik H. B., 2007, *MNRAS*, 375, 958
- Diego J. M., et al., 2015, *MNRAS*, 446, 683
- Diego J. M., et al., 2016, *MNRAS*, 456, 356
- Diego J. M., et al., 2023a, *A&A*, 679, A31
- Diego J. M., et al., 2023b, *A&A*, 679, A159
- Diego J. M., et al., 2024, *A&A*, 689, A167
- Diego J. M., et al., 2025, *arXiv e-prints*, p. arXiv:2506.11207
- Eid L., Keeton C. R., 2025, *ApJ*, 990, 196
- Euclid Collaboration et al., 2025, *arXiv e-prints*, p. arXiv:2503.15330
- Frye B. L., et al., 2024, *ApJ*, 961, 171
- Fudamoto Y., et al., 2024, *arXiv e-prints*, p. arXiv:2404.08045
- Galan A., Van de Vyvere L., Gomer M., Vernardos G., Sluse D., 2023, *The Journal of Open Source Software*, 8, 5567
- Galan A., Caminha G. B., Knollmüller J., Roth J., Suyu S. H., 2024a, *arXiv e-prints*, p. arXiv:2402.18636
- Galan A., Vernardos G., Minor Q., Sluse D., Van de Vyvere L., Gomer M., 2024b, *A&A*, 692, A87
- Granata G., et al., 2025, *A&A*, 697, A94
- Griffiths R. E., Rudisel M., Wagner J., Hamilton T., Huang P.-C., Villforth C., 2021, *MNRAS*, 506, 1595
- Ishigaki M., Kawamata R., Ouchi M., Oguri M., Shimasaku K., Ono Y., 2015, *ApJ*, 799, 12
- Jauzac M., et al., 2012, *MNRAS*, 426, 3369
- Jauzac M., et al., 2014, *MNRAS*, 443, 1549
- Johnson T. L., Sharon K., Bayliss M. B., Gladders M. D., Coe D., Ebeling H., 2014, *ApJ*, 797, 48
- Johnson T. L., et al., 2017a, *ApJ*, 843, 78
- Johnson T. L., et al., 2017b, *ApJL*, 843, L21
- Joye W. A., Mandel E., 2003, in Payne H. E., Jedrzejewski R. I., Hook R. N., eds, *Astronomical Society of the Pacific Conference Series Vol. 295, Astronomical Data Analysis Software and Systems XII*. p. 489
- Jullo E., Kneib J. P., Limousin M., Elíasdóttir Á., Marshall P. J., Verdugo T., 2007, *New Journal of Physics*, 9, 447
- Karchev K., Coogan A., Weniger C., 2022, *MNRAS*, 512, 661
- Kawamata R., Oguri M., Ishigaki M., Shimasaku K., Ouchi M., 2016, *ApJ*, 819, 114
- Kawamata R., Ishigaki M., Shimasaku K., Oguri M., Ouchi M., Tanigawa S., 2018, *ApJ*, 855, 4
- LSST Science Collaboration et al., 2009, *arXiv e-prints*, p. arXiv:0912.0201
- Lasko K., Williams L. L. R., Ghosh A., 2023, *MNRAS*, 525, 5423
- Liesenborgs J., de Rijcke S., Dejonghe H., Bekaert P., 2007, *MNRAS*, 380, 1729
- Liesenborgs J., Perera D., Williams L. L. R., 2024, *MNRAS*, 529, 1222
- Limousin M., et al., 2025, *A&A*, 693, A33
- Lin J., Wagner J., Griffiths R. E., 2023, *MNRAS*, 526, 2776
- Lotz J. M., et al., 2017, *ApJ*, 837, 97
- Lucy L. B., 1974, *AJ*, 79, 745

- Navarre A., et al., 2024, *ApJ*, 962, 175
- Niemiec A., et al., 2023, *MNRAS*, 524, 2883
- Nightingale J. W., Dye S., 2015, *MNRAS*, 452, 2940
- Oguri M., 2010, *PASJ*, 62, 1017
- Patrício V., et al., 2018, *MNRAS*, 477, 18
- Pedregosa F., et al., 2011, *Journal of Machine Learning Research*, 12, 2825
- Pierel J. D. R., et al., 2025, arXiv e-prints, p. arXiv:2509.12301
- Raney C. A., Keeton C. R., Brennan S., 2020a, *MNRAS*, 492, 503
- Raney C. A., Keeton C. R., Brennan S., Fan H., 2020b, *MNRAS*, 494, 4771
- Richard J., Kneib J. P., Limousin M., Edge A., Jullo E., 2010, *MNRAS*, 402, L44
- Richard J., et al., 2014, *MNRAS*, 444, 268
- Richardson W. H., 1972, *Journal of the Optical Society of America (1917-1983)*, 62, 55
- Rüstig J., Guardiani M., Roth J., Frank P., Enßlin T., 2024, *A&A*, 682, A146
- Sarrouh G. T. E., et al., 2025, arXiv e-prints, p. arXiv:2506.21685
- Shajib A. J., et al., 2025, *Philosophical Transactions of the Royal Society of London Series A*, 383, 20240117
- Sharon C. E., et al., 2019, *ApJ*, 879, 52
- Soucail G., 1987, *The Messenger*, 48, 43
- Soucail G., Fort B., Mellier Y., Picat J. P., 1987, *A&A*, 172, L14
- Soucail G., Mellier Y., Fort B., Mathez G., Cailloux M., 1988, *A&A*, 191, L19
- Suyu S. H., Marshall P. J., Hobson M. P., Blandford R. D., 2006, *MNRAS*, 371, 983
- Tagore A. S., Jackson N., 2016, *MNRAS*, 457, 3066
- Tagore A. S., Keeton C. R., 2014, *MNRAS*, 445, 694
- Tessore N., Bellagamba F., Metcalf R. B., 2016, *MNRAS*, 463, 3115
- Vega-Ferrero J., Diego J. M., Bernstein G. M., 2019, *MNRAS*, 486, 5414
- Vegetti S., Koopmans L. V. E., 2009, *MNRAS*, 392, 945
- Vernardos G., Koopmans L. V. E., 2022, *MNRAS*, 516, 1347
- Virtanen P., et al., 2020, *Nature Methods*, 17, 261
- Warren S. J., Dye S., 2003, *ApJ*, 590, 673
- Yang L., Birrer S., Treu T., 2020, *MNRAS*, 496, 2648
- Young A. J., Keeton C. R., Baker A. J., 2022, *ApJ*, 929, 6
- Şengül A. Ç., 2025, *A&A*, 699, A47
- Şengül A. Ç., Birrer S., Natarajan P., Dvorkin C., 2023, *MNRAS*, 526, 2525